Article ID：1007−7294(2025)06−0924−17

Numerical Analysis on Influence of Preset Bubble in a Fluid-filled Structure on the Characteristics of Projectile Penetration and Structural Failure

WU Meng−meng[a,b], *HOU Hai−liang*[a], *LI Dian*[a], *LI Yong−qing*[a], *XIA Wei−xue*[b], *YANG Shao−hong*[b]
(a. College of Naval Architecture and Ocean Engineering; b. Department of Basic Courses, Naval University of Engineering, Wuhan 430033, China)

Abstract: In this paper, the failure caused by HRAM loads which were generated by high-speed projectile penetration, and protection technology of the fluid-filled structure were explored. A bubble was preset on the projectile trajectory in a fluid-filled structure. Based on the reflection and transmission phenomena of pressure waves at the gas-liquid interface and the compressibility characteristics of gases, a numerical analysis was conducted on the influence of preset bubble on projectile penetration and structural failure characteristics. The results indicate that the secondary water-entry impact phenomenon occurs when a preset bubble exists on the projectile trajectory, leading to the secondary water entry impact loads. The rarefaction waves reflected on the surface of the preset bubble cause the attenuation ratio of the initial impact pressure peak to reach 68.8% and the total specific impulse attenuation ratio to reach 48.6%. Furthermore, the larger the bubble, the faster the projectile, and the more obvious the attenuation effect. Moreover, due to the compressibility of the bubble, the global deformation attenuation ratio of the front and rear walls can reach over 80%. However, the larger the bubble size, the faster the projectile velocity, the smaller the local deformation attenuation effect of the rear wall, and the more severe the failure at the perforation of the rear wall.

Key words: fluid-filled structure; preset bubble; HRAM loads; projectile; penetration; attenuation
CLC number：O342 **Document code**：A **doi:** 10.3969/j.issn.1007−7294.2025.06.007

0 Introduction

The impact and penetration of projectiles into fluid-filled structures may cause catastrophic consequences. There are many scenarios such as the impact and penetration of high-speed fragments into aircraft fuel tanks[1], the impact and penetration of spacecraft pressure vessels by space debris[2], and shooting of flammable or toxic liquid storage tanks[3] by terrorists. The impact and penetration of the projectile will generate a hydrodynamic ram (HRAM) effect in a fluid-filled structure, forming strong pressure waves and liquid flow. This effect, combined with the projectile's effect, will cause large-scale fractures or bursts in the structure. Effectively controlling or alleviating the HRAM loads formed by high-speed projectile penetration

Received date：2024−12−24
Foundation item：Supported by the National Natural Science Foundation of China (52271338; 51979277; 52371342; 12102475)
Biography：WU Meng-meng(1991–), female, Ph. D. candidate, lecturer, corresponding author, E-mail: mengmengwu1017@163.com; HOU Hai-liang(1977–), male, Ph. D., professor.

while ensuring the integrity of fluid-filled structures has become an important direction of aircraft fuel tanks and other fluid-filled structures in the projectile resistance and protection design.

There are two main mechanisms for attenuating the HRAM effect in fluid-filled structures: impediment and load-off. Impediment refers to setting rigid bodies and energy-absorbing structures that disturb pressure waves along the transmission path. These bodies impede the direct action of HRAM loads on the inner wall of the fluid-filled structures, achieving attenuation and dissipation of HRAM loads. Disimile et al[4] installed four different geometries of triangular bars in the fluid-filled structure to reflect the shock wave and thus alleviate its failure effect on the subsequent structure. The experimental results showed that the peak pressure on the rear wall of the fluid-filled structure with the pressure mitigation system was reduced by 60% compared to that in the absence of the shock mitigating members. Wang et al[5] and Artero-Guerrero et al[6] conducted penetration experiments on novel perforated lattice fluid-filled structures and honeycomb aluminum structures, and found that the core layer's deformation and energy absorption process weakened the HRAM loads and reduced the bulging deformation of the outer wall of the fluid-filled structures. On this basis, Xu et al[7] embedded aramid fiber tubes in the honeycomb aluminum structure. The HRAM energy was simultaneously absorbed by the aramid tubes and honeycomb aluminum structure. Thereby, the HRAM loads were further weakened, and the ability of penetration resistance was improved. Objectively speaking, the above measures impede the HRAM loads but also increase the weight of the structures and reduce the fluid-filled capacity.

Load-off refers to installing compressible partitions within the fluid-filled structure or using the deformation characteristics of the fluid-filled structure to guide the directional release of HRAM loads, achieving attenuation and dissipation of the HRAM effect. Gao et al[8] and Zhao et al[9] proposed a fluid-filled structure with concave cells that utilized the pressure relief space provided by the structure when transitioning from concave to convex state under HRAM loads to release pressure and reduce the load acting on the fluid-filled structure. The authors proposed the concept of expansion impedance[10], which was used to measure the difficulty of expansion of a fluid-filled structure. The more easily the structure expands, the smaller the HRAM loads it bears. Varas et al[11−13] and Artero-Guerrero et al[14] explored the influence of filling levels in fluid-filled structures subjected to high-velocity impacts using experimental and simulation methods. The results indicate that the fluid moves towards the walls only in the region close to the projectile trajectory under incomplete filling. The fluid expands in parallel with the walls at larger distances through the unfilled volume. Therefore, low filling levels cause localization of the permanent deformation in the tube at regions close to the projectile trajectory.

Furthermore, Zhang et al[15] investigated the influence of fluid-filled capacity on the anti-penetration performance of the fluid-filled grid structure, and found that reducing fluid-filled capacity leads to additional cavitation expansion. Therefore, the strength of the cavitation extrusion load acting on the inner plate is weakened. Townsend et al[16] used the difference in wave impedance between gas-liquid materials to disturb and disperse the initial pressure wave by arranging thin air baffles and compressing bubbles within the fluid-filled structure. This process significantly reduced the pressure and structural failure of the fluid-filled structure. Li et al[17] installed an air interlayer inside the fluid-filled structure, reducing the front and rear walls' impulse, energy, and plastic deformation under high-speed projectile penetration. Jin et al[18] proposed a preset bubble inside the fluid-filled structure, reflecting sparse waves through the compressibility of the preset bubble and providing motion space for the fluid by changing the pressure environment of the flow field. Furthermore, the authors alleviated the failure of the fluid-filled structure under HRAM loads. However, the

projectile will pass through the air during penetration as the air barriers and bubbles are preset in the fluid-filled structure, resulting in a smaller penetration distance in the fluid and a higher residual velocity, which makes it easier to penetrate the fluid-filled structure. Researchers have mainly focused on the attenuation of HRAM loads and the protective effect of structure by preset bubbles. They have not considered the influences on penetration ability and failure characteristics of fluid-filled structures caused by passing through air during penetration.

This paper presents an investigation of the influences on the penetration ability of the projectile and the failure characteristics of the fluid-filled structure when a projectile passes through a preset bubble during penetrating fluid-filled structure, based on the experimental model of a spherical projectile penetrating the fluid-filled structure in Ref. [11]. The explicit dynamic analysis software LS-DYNA is used to conduct the numerical analysis and explore the influences of preset bubbles on the penetration path to impact load. The structural deformation and failure characteristics during the projectile penetration of the fluid-filled structure are also explored.

1 Numerical simulation

1.1 Computation model

The fluid-filled structure in the ballistic experiment in Ref. [11] was taken as the object. Numerical analysis was carried out to investigate the effect of the preset bubble on the penetration process of a projectile, the resulting HRAM loads, structural deformation and failure characteristics. The structural dimensions and two pressure transducers inside the water are shown in Fig. 1. The fluid-filled structure comprised 6063-T5 square aluminum tubes of 150 mm in width, 2.5 mm in thickness, and 750 mm in length. The specimens were closed with two PMMA windows with a thickness of 30 mm. The contact points between PMMA windows and specimens were sealed with silicone to avoid fluid leakage. The projectile to be launched against the fluid-filled structure was a steel sphere with a diameter of 12.5 mm and a mass of 8 g. The preset bubble diameter was *D,* arranged in the center of the fluid-filled structure.

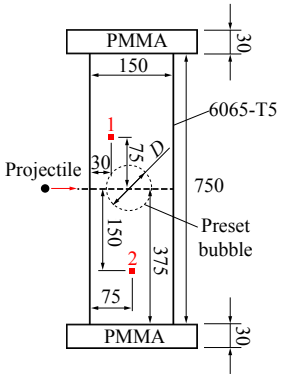

Fig.1 Sketch of the impact tests device (Units: mm)

1.2 Pressure gauges and calculation cases

A total of 13 pressure gauges in different positions of the fluid and near the walls were selected for pressure and load analysis, as is shown in Fig. 1 and Fig. 2. Pressure Gauges 1 and 2 were located in the fluid to validate the effectiveness of numerical simulation and analyze the pressure characteristics of the free field in the water. According to the different load characteristics, the front and rear walls of the fluid-filled structure under high-speed projectile penetration could be both divided into three areas[19]. Area a was the impact zone of the projectile, whose radius R_1 was equal to 12.5 mm. Area b was the maximum cavitation zone. The maximum cavitation radius of the front (R_f) and rear (R_b) walls was equal to 50 mm and 30 mm, respectively. Area c was the remaining area. Pressure Gauges 3–5 were placed in areas a, b, and c of the front wall to analyze its load characteristics. Pressure Gauges 6–8 were placed in areas a, b, and c of the rear wall

to analyze its load characteristics. Next, the region influenced by different preset bubble sizes on the initial and secondary impact pressure waves was analyzed. Starting from the projectile's impact point, tangent lines were drawn through bubbles and extended to the rear wall, forming a projection region of bubbles of different sizes on the rear wall. Five typical pressure gauges were selected inside and outside the projection region, marked as 9–13.

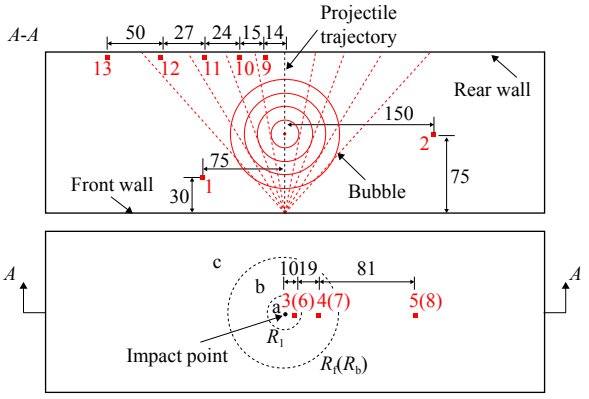

Fig.2 Arrangement of pressure gauges (Units: mm)

A total of 13 simulation cases were calculated and analyzed by considering the influence of projectile velocity and bubble size on the penetration process, the structural deformation and failure characteristics, as shown in Tab. 1. Cases 1−5 and 6−10 were used to analyze the penetration phenomena without and with preset bubbles at different projectile velocities while Cases 3, 8, 11−13 were mainly used to analyze the influence of bubble size on the projectile penetration, structural deformation and failure characteristics.

Tab.1 Simulation cases for different bubble sizes and projectile velocities

Simulation cases	Bubble diameter/mm	Projectile velocity/(m·s^{-1})	Simulation cases	Bubble diameter/mm	Projectile velocity/(m·s^{-1})
Case 1	0	180	Case 8	100	900
Case 2	0	600	Case 9	100	1100
Case 3	0	900	Case 10	100	1600
Case 4	0	1100	Case 11	25	900
Case 5	0	1600	Case 12	50	900
Case 6	100	180	Case 13	75	900
Case 7	100	600			

1.3 Meshing and convergence analysis

Symmetric boundary conditions were applied to the model, as shown in Fig. 3. The projectile, walls of the fluid-filled structure, and the PMMA were discretized via eight-node solid Lagrangian elements. The Euler domain extended 50 mm outward from the inner wall of the fluid-filled structure to ensure that the fluid-filled structure would always be within the Euler domain and the conservation of system energy[20]. The Johnson-Cook constitutive model, failure mode, and the Gruneisen Equation of State were adopted for the fluid-filled structure. The relevant parameters were the same as those in Ref. [12].

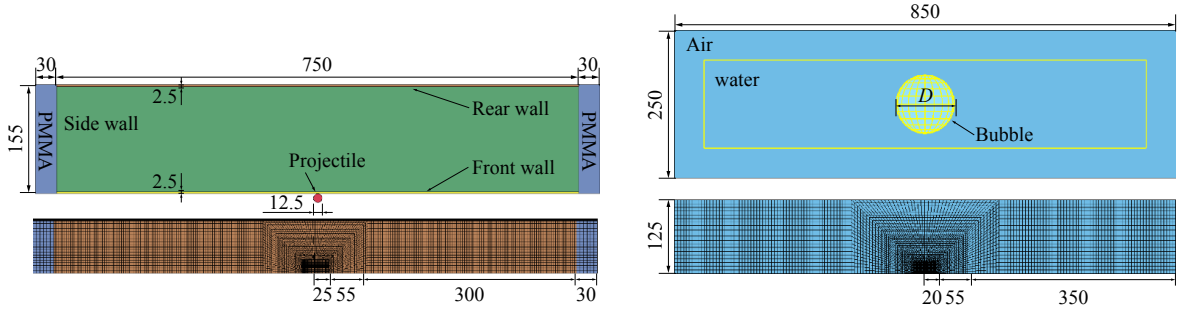

（a）Mesh of the structure　　（b）Mesh of the fluids

Fig.3 Sketch of 1/2 symmetric fluid-filled structure meshing

A refined mesh was used in the impact zone, and a coarser mesh was used in areas far away from the impact zone, as shown in Fig. 3. A fine grid was used within the range of 0–20 mm from the projectile trajectory, a medium transition grid was used within the range of 20–75 mm, and a coarse grid was used in the remaining areas.

The influence of the bonding strength between aluminum walls and PMMA was ignored to ensure the integrity of the fluid-filled structure. Common nodes were carried out at the junction of each wall and PMMA. The boundary conditions of the Euler domain and its outermost part were non-reflective.

The coarse, fine and transitional grid size ratios were kept constant. Then, six different grid sizes were used in the center fine grid (with sizes of 6 mm, 4 mm, 1.6 mm, 1 mm and 0.8 mm, respectively) to obtain the grid size when the calculation results converged.

Fig. 4 depicts the peak pressure at Gauge 1 and displacement curves of the mid-section centerline of the front and rear walls. It can be seen that when the fine grid size is 1 mm, the peak pressure at Ggauge 1 and the front and rear wall deformation have converged. Therefore, the fine grid size required for the fluid-filled structure is 1 mm, while the transition zone grid size is 3 mm and the coarse grid size is 5 mm. The grid size of the projectile is the same as that of the contact area related to the fluid-filled structure, namely 1 mm. The front, rear, and side walls are divided into five grid layers in the thickness direction. The final mesh of the structure comprised 573 552 elements.

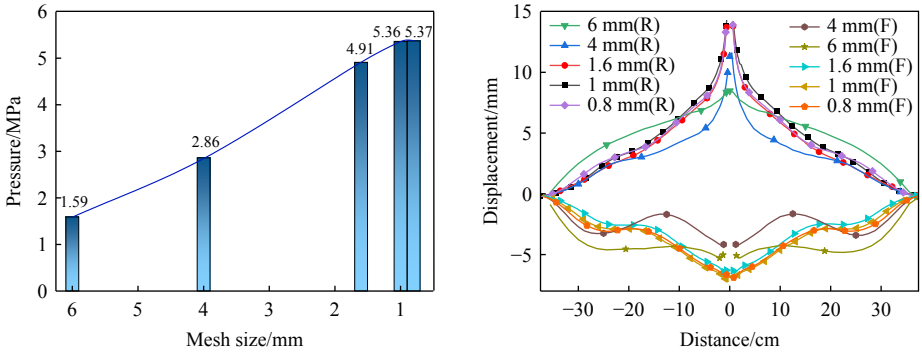

（a）Pressure peak of Gauge1　　（b）Centerlines displacement of the front and rear walls

Fig.4 Grid convergence analysis

1.4 Numerical model validation

Fig. 5 depicts the experimental and numerical results of the longitudinal profile shape and dimensions of the cavitation formed by projectile penetration at typical moments in Case 2. Among them, the cavitation dimensions in the experimental results are proportionally converted from the distance between Pressure Gauges 1 and 2. The instantaneous moment of the projectile shear plug front wall is taken as the zero moment of the cavitation in the simulation. According to Fig. 5, the longitudinal profile shape of the cavitation in the simulation matches the experiment. Typical cross-sectional dimensions of the cavitation (30 mm away from the front wall) are slightly smaller than thoze of the experiment.

Fig. 6 depicts the experimental and numerical calculation results of the time history curves of Pressure Gauges 1 and 2 in Case 2, as well as the displacement curves of the mid-section centerline of the front and rear walls. It is shown that the variation process of Pressure Gauges 1 and 2 in numerical calculation is consistent with the experimental results. The deviation of the peak pressure of Gauges 1 and 2 between the simulation and experimental results is 2.2% and 24.5%, respectively. The main reason for the difference of Pressure Gauges 2 is more significant is that Pressure Gauge 2 is located in the transitional grid area, where

the grid size is slightly larger. The calculation results of the front and rear walls in the impact area of the projectile agree with the experimental results. But the calculation results are biased in the boundary area near both sides due to the difference in boundary conditions.

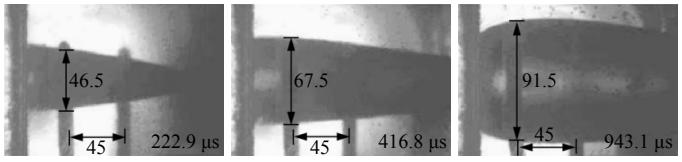

（a）High-speed photos[11]

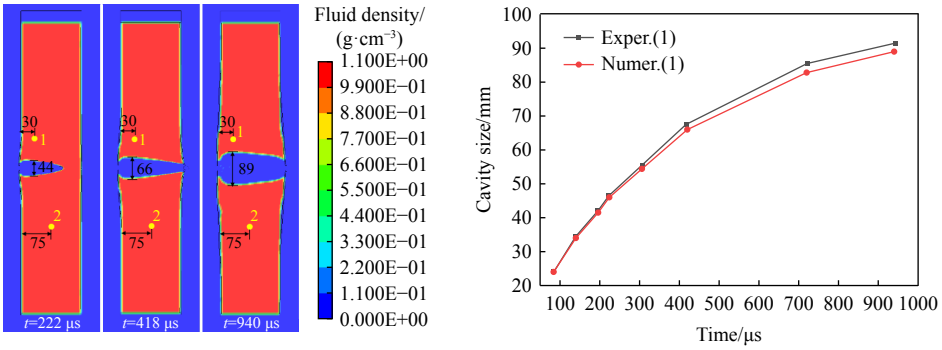

（b）Numerical results　　（c）Cavity size

Fig.5 Comparison of the shape and dimension of cavitation zone between experimental and numerical results (Units: mm)

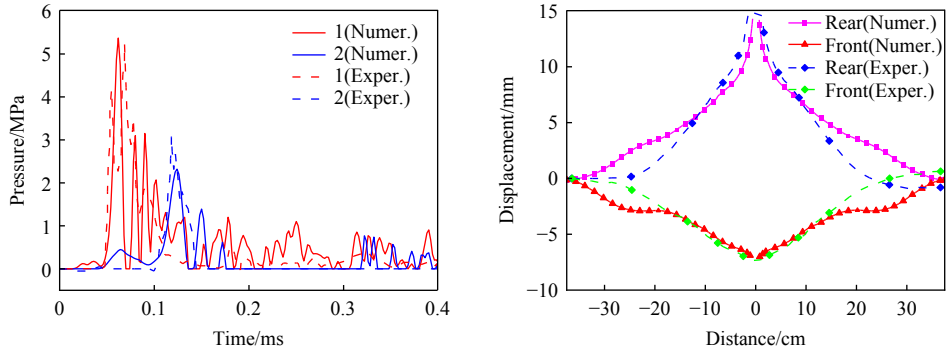

（a）Pressure　　（b）Centerlines displacement

Fig.6 Comparison of pressure of Gauges 1 and 2 and centerlines displacement of the front and rear walls between experimental and numerical results

2 Numerical simulation results and analysis

2.1 Influence of preset bubble on physical processes

Cases 2 and 7 were taken to analyze the effects of preset bubbles in the fluid-filled structure on physical processes such as projectile penetration, pressure wave propagation and cavitation expansion. The dynamic response characteristics, such as projectile velocity attenuation, penetration distance and structural deformation, were also considered.

2.1.1 Projectile penetration and pressure wave propagation

The projectile penetration and pressure wave propagation could be divided into five stages in Case 2[21]. Fig. 7 depicts the density variation in the Euler domain at a typical moment on the horizontal cross-section of

the fluid-filled structure in Case 7. In the figure, the density variation range of the Euler domain was set to 0.998–1.002 g/cm^3 to obtain the pressure variation and cavitation process during projectile penetration. Fig. 8 depicts the time history curves of Pressure Gauges 1 and 2 in Cases 2 and 7.

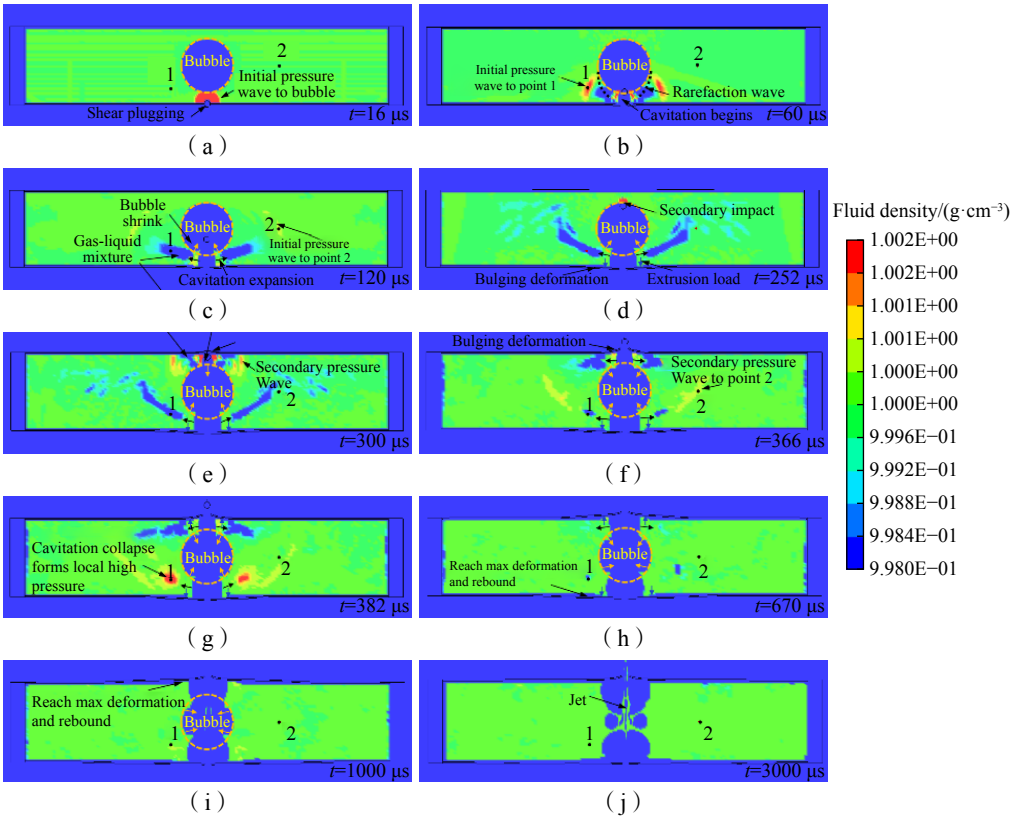

Fig.7 Changes in Euler domain density with preset bubble

With a preset bubble, the projectile penetration and pressure wave propagation can be divided into six stages:

(1) Initial impact stage. When the projectile penetrates the front wall of the fluid-filled structure, the fluid is rapidly compressed to form a hemispherical pressure wave. The impact energy of the projectile is converted into the compression potential energy of the fluid. Since penetration of the projectile in the fluid is subsonic, the initial pressure wave gradually separates from the projectile and propagates outward, as is shown in Fig. 7(a).

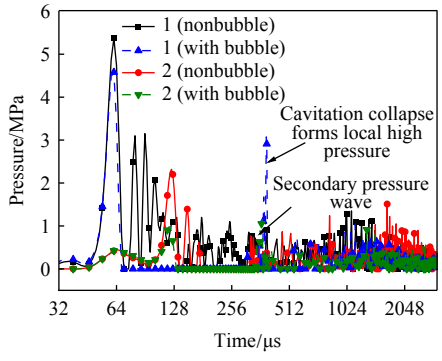

Fig.8 Comparison of time history curves at Pressure Gauges 1 and 2

(2) Drag and cavitation stage. Since the velocity of the fluid in front of the projectile is lower than that behind it, the projectile is slowed by viscous drag. A cavitation zone is formed behind the projectile as the fluid moves radially. Simultaneously, a long-term pressure with a smaller amplitude is formed in the fluid. At 16 μs, the initial impact pressure wave propagates to the bubble's surface, and the bubble starts to shrink and deform from the compressed side. As the cavitation in front of the bubble continues to expand, the shrinkage and deformation of the front surface of the bubble become more obvious. Due to the compressibility of the

bubble, the fluid's extrusion load on the front wall decreases. Furthermore, the bulging deformation of the front wall decreases, as shown in Fig. 7(b).

Pressure waves reflect rarefaction waves on the bubble's surface and form a low-pressure zone in front of the bubble due to the huge impedance difference between gas and fluid. The pressure in the low-pressure zone is lower than the gasification pressure of water, forming a cavitation zone of a gas-liquid mixture (the low-pressure zone appears blue like a bubble in Fig. 7(c); its density is only lower than the minimum chromatographic value of 0.998 g/cm^3 and still much higher than the air density). The rarefaction waves reflected on the bubble's surface reduce the pressure wave's peak strength. Hence, the propagation of pressure waves is invisible behind the bubble. At 60 μs, the pressure wave front propagates to Pressure Gauge 1 with a peak pressure of 4.58 MPa, which is reduced by 15% compared to the case without a preset bubble, as shown in Fig. 8.

(3) Bubble penetration stage. After 60 μs, the projectile enters the bubble, and its velocity hardly decays (Fig. 10). The projectile's kinetic energy is no longer transformed into the fluid. Moreover, the cavitation on the front of the bubble continues to expand under the inertial effect, compressing the shrinkage of the front surface of the bubble. At 120 μs, the initial pressure wavefront propagates to Pressure Gauge 2 (Fig. 7(c)). A peak pressure of 0.91 MPa is reduced by 15% compared to that without the preset bubble, as shown in Fig. 8.

(4) Secondary impact stage. After 252 μs, the projectile penetrates the bubble and enters the water again, generating a secondary spherical pressure wave that propagates forward and forms secondary cavitation behind the bubble (Fig. 7(d)). The secondary pressure wave mainly acts on the local zone of the rear wall and quickly forms a reflection wave at the rear wall due to the small distance between the back surface of the bubble and the rear wall. Therefore, a low-pressure zone is formed again in the rear wall, resulting in a cavitation zone of a gas-liquid mixture. At 300 μs, the projectile reaches the rear wall and undergoes dishing deformation in a local zone (Fig. 7(e)). As the cavitation near the rear wall expands, the rear wall undergoes bending deformation under extrusion load. Simultaneously, the surface behind the bubble begins to shrink.

(5) Exit stage. At 350 μs, the projectile penetrates the rear wall and exits the fluid-filled structure (Fig. 7(f)).

(6) The cavitation collapse stage. Once the projectile exits, the secondary pressure wave propagates in the fluid. At 366 μs, the secondary pressure wave reaches Pressure Gauge 2, generating a peak pressure of 1.16 MPa (Fig. 7(g)). At 382 μs, the local cavitation collapse at Pressure Gauge 1 generates a high local pressure, with a peak value of up to 3.08 MPa (Fig. 8). At 670 μs, the cavitation near the front wall reaches its maximum size and no longer expands, resulting in the maximum deformation of the front wall (Fig. 7(h)). At 1000 μs, the cavitation near the rear wall reaches its maximum size and no longer expands, resulting in maximum deformation of the rear wall (Fig. 7(i)). Then, since the pressure inside the cavitation is lower than the external atmospheric pressure, the water around starts to flow toward the cavitation. Moreover, the bubble rapidly contracts and collapses along the radial direction, producing an upward jet (Fig. 7(j)). The front and rear walls rebound to the final deformation position.

In summary, with a preset bubble, the initial pressure waves reflect rarefaction waves on the bubble's surface, attenuating its strength in the fluid. The secondary impact pressure wave is formed once the projectile exits the bubble and enters the water again. Moreover, the preset bubble divides the cavitation expansion process into two parts: in front of the bubble and behind the bubble.

2.1.2 Analysis of the position and velocity attenuation of the projectile

A projectile's motion in the fluid can be inferred from Ref. [22]. Once the preset bubble is located on the

projectile's trajectory, the projectile's penetration process in the fluid-filled structure can be divided into three stages: Stage I—Initial Water Entry, Stage II—Penetration Bubble, and Stage III—Secondary Water Entry. In Stage II, the projectile is almost not dragged, β can be regarded as 0, and the velocity and position expressions of the projectile can be expressed in stages as follows:

$$\begin{cases} \dfrac{1}{v_{\mathrm{pI}}}-\dfrac{1}{v_0}=\beta t, & t\leqslant t_{\mathrm{I}} \\ v_{\mathrm{pII}}=Const, & t_{\mathrm{I}}<t\leqslant t_{\mathrm{II}} \\ \dfrac{1}{v_{\mathrm{pIII}}}-\dfrac{1}{v_{\mathrm{pII}}}=\beta(t-t_{\mathrm{II}}), & t_{\mathrm{II}}<t\leqslant t_{\mathrm{III}} \end{cases}, \tag{1}$$

$$\begin{cases} z_{\mathrm{pI}}=\dfrac{1}{\beta}\ln(v_0\beta t+1), & t\leqslant t_{\mathrm{I}} \\ z_{\mathrm{pII}}=v_{\mathrm{pII}}(t-t_{\mathrm{I}})+z_{\mathrm{pI}}, & t_{\mathrm{I}}<t\leqslant t_{\mathrm{II}} \\ z_{\mathrm{pIII}}=z_{\mathrm{pII}}+\dfrac{1}{\beta}\ln(v_{\mathrm{pIII}}\beta(t-t_{\mathrm{II}})+1), & t_{\mathrm{II}}<t\leqslant t_{\mathrm{III}} \end{cases}, \tag{2}$$

where t_{I} is the moment when the projectile penetrates the bubble, t_{II} is the moment when the projectile exits the bubble and enters water, and t_{III} is the moment when the projectile reaches the rear wall. Parameters v_{pI} and z_{pI} represent the velocity and position of the projectile in Stage I, respectively; v_{pII} and z_{pII} are the velocity and position of the projectile in Stage II, respectively; v_{PIII} and z_{pIII} are the velocity and position of the projectile in Stage III, respectively.

Comparison of the analysis results with the numerical calculation results (Figs. 9(a) – (b)) reveals good consistency. With a preset bubble, the penetration time of the projectile in the fluid-filled structure is shortened, the velocity attenuation is reduced, and the remaining velocity increases. Hence, a three-stage formula can be used to calculate its velocity attenuation.

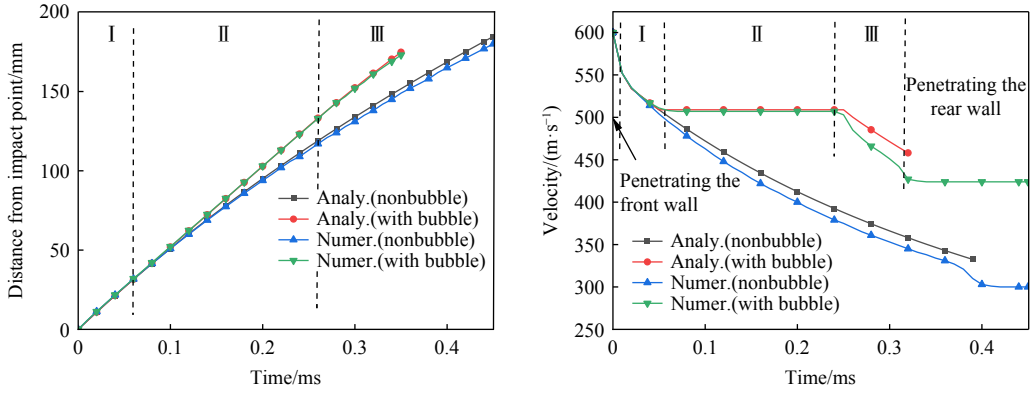

（a）Variation of penetration distance versus time （b）Variation of velocity versus time

Fig.9 Comparison between of analytical and numerical results for penetration with and without bubble

2.1.3 Analysis of load characteristics and deformation failure modes of front and rear walls

Pressure Gauges 3–8 in the front and rear walls within a, b, and c zones of Cases 2 and 7 were taken (Fig. 2). A comparison of the pressure time history curves and specific impulse is shown in Figs. 10 and 11.

As shown in Fig. 10, in addition to the projectile impact, the front wall is also subjected to initial impact pressure wave and cavitation extrusion load, with pressure peaks of P_{f} and P_{c}, respectively. The cavitation extrusion load P_{c} is the average value of the entire load process after the initial impact pressure wave[19].

In the process of the projectile shearing and punching the front wall, Zone *a* is affected by a larger incident pressure wave. The preset bubble does not affect this region's load characteristics and specific impulse (Fig. 10(a)). Cavitation forms and gradually expands as the penetration distance of the projectile

increases. The initial impact pressure peak is unaffected in Zones *b* and *c* because the incident pressure wave arrives before the reflected rarefaction wave. However, the compressibility of the preset bubble reduces the cavitation extrusion load and specific impulse in Zones *b* and *c*. The attenuation ratios of the cavitation extrusion load and specific impulse in Zone *b* are 40.6% and 28.7%, respectively. The cavitation extrusion load and specific impulse attenuation ratios in Zone *c* are 38.2% and 42.3%, respectively (Figs. 10(b) and (c)).

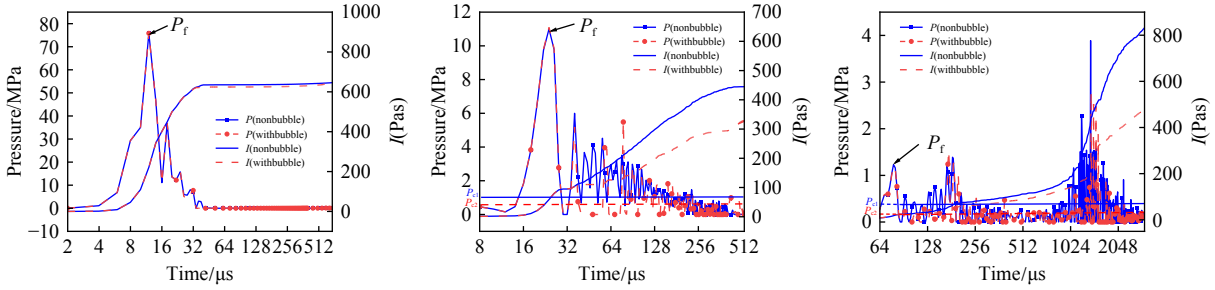

（a）Zone *a*　（b）Zone *b*　（c）Zone *c*

Fig.10 Load characteristics of the front wall

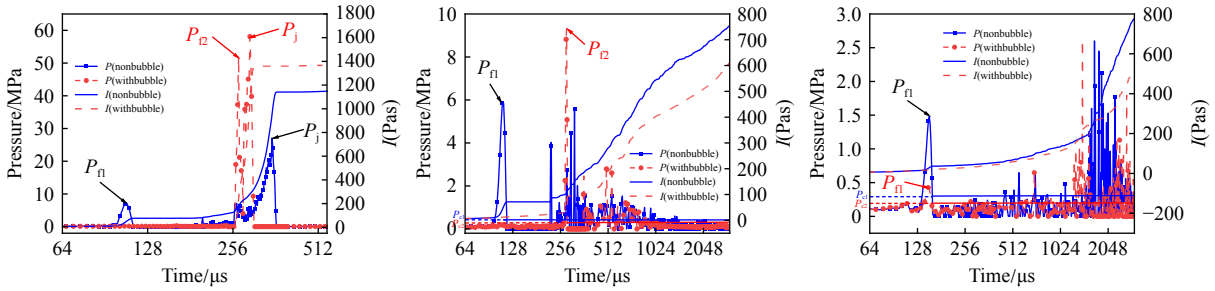

（a）Zone *a*　（b）Zone *b*　（c）Zone *c*

Fig.11 Load characteristics of the rear wall

As shown in Fig. 11, the impact loads on the rear wall are mainly the initial impact pressure wave, secondary impact pressure wave, local high pressure, and cavitation extrusion load, with peak pressure values of P_{f1}, P_{f2}, P_j, and P_c, respectively.

As we can see, the pressure load in Zone *a* of the rear wall remained almost zero, but in the later stage, a pressure peak reached up to 50–60 MPa. The load in Zone *b* also has similar characteristics, but the pressure peak in the later stage is only about 9 MPa. The reason is that the preset bubble is located directly in front of Zone *a*, effectively blocking the pressure wave formed by the initial water entry of the projectile. In the later stage, the projectile passes through the preset bubble and enters the water again, forming a pressure wave that acts on Zones *a* and *b*. The initial impact pressure wave in Zone *c* is also significantly weakened, with a peak value reduced from 1.48 MPa to 0.41 MPa, representing a decrease of 72.3%. Zones *a* and *b* are subjected to the secondary impact pressure wave caused by the projectile penetration of the bubble, with peak values reaching 52.3 MPa and 9.32 MPa, respectively. The influence range of the secondary impact pressure wave is relatively small due to the small distance between the back surface of the bubble and the rear wall of the fluid-filled structure. The cavitation extrusion load in Zone *c* is significantly reduced due to the high compressibility of the bubble, with an average value and specific impulse decrease of 28.9% and 34.7%, respectively.

Moreover, it can be seen from Fig. 10(c) and Fig. 11(c) that in the zone *c* of the front and rear walls, the

pressure time history curve exhibits high-frequency vibration in the later stage, which is due to the local high pressure generated by cavitation collapse in the liquid. After preset bubble, it also has an attenuating effect on local cavitation phenomena.

In light of the results previously shown, it can be concluded that the front wall will be subjected to loads such as projectile penetration, initial impact pressure wave, and cavitation extrusion load when projectiles penetrate the fluid-filled structure. In contrast, the rear wall will be subjected to loads such as initial impact pressure wave, secondary impact pressure wave, cavitation extrusion load, local high pressure, and projectile penetration. According to the relative region of the load range, these loads can be roughly divided into local and global loads; their relative strength will vary with changes in projectile velocity, preset bubble, and other factors.

Therefore, the deformation and failure modes of the front and rear walls of the fluid-filled structure under projectile penetration are divided into global and local failures, as shown in Fig. 12. The global deformation range extends to the boundary of the wall characterized by bulging deformation and tearing failure boundary. The curvature is convex and mainly formed by the combined action of the initial impact pressure wave, cavitation extrusion load, and other global loads. The local failure range is relatively small and mainly concentrated near the projectile's impact point, characterized by shearing and plugging, reverse dishing deformation, and petal cracking. The curvature is concave and mainly formed by local loads such as projectile penetration and local high pressure at the projectile head.

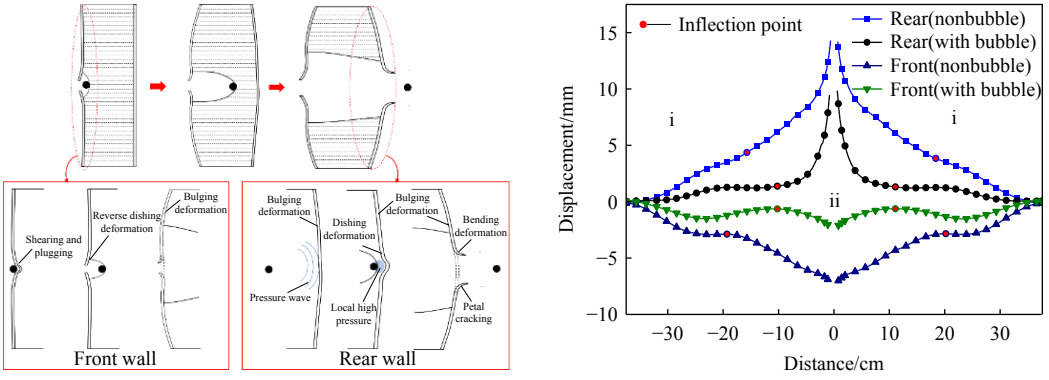

（a）Deformation and failure modes （b）Centerline displacement

Fig.12 Sketch of deformation and failure modes and the centerline displacement of front and rear walls

Fig. 13 depicts the displacement curves of the front and rear walls along the centerline in Cases 2 and 7. The front and rear walls' global deformation zone i and local deformation zone ii are distinguished based on the curve curvature transition point from convex to concave. With a preset bubble, the maximum global deformation of the front and rear walls (the maximum value of the global deformation zone) decayed from 2.91 mm and 4.37 mm to 1.5 mm and 1.27 mm respectively, with attenuation ratios of 48.5% and 70.9%, accordingly. The maximum local deformation (the maximum value of the local deformation zone minus deformation value at the inflection point) decayed from 4.13 mm and 9.93 mm to 1.41 mm and 8.45 mm, respectively, with attenuation ratios of 66.3% and 14.9%. It can be concluded that a preset bubble significantly reduces the maximum global deformation of the front and rear walls, as well as the local deformation of the front wall. The attenuation ratio of the local deformation of the rear wall is relatively small. Moreover, the range of local deformation of the front and rear walls is reduced.

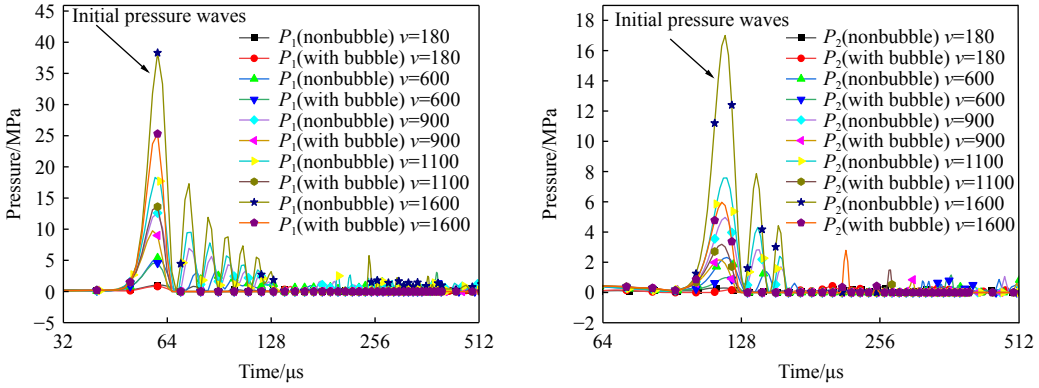

Fig.13 Time history curves of Pressure Gauges 1 and 2 at different velocities

2.2 Attenuation effect at different projectile velocities

2.2.1 Analysis of pressure attenuation characteristics

Fig. 13 shows a comparison of time history curves at Pressure Gauges 1 and 2 under different velocities. In order to clarify the attenuation effect of preset bubble on initial impact pressure wave under different velocities, the attenuation of the initial impact pressure wave peak and total specific impulse (t = 3000 μs) at Pressure Gauges 1 and 2 in Cases 1–10 are compared in Fig. 14 to investigate the effects of the reflection of rarefaction waves on the surface of the preset bubble and its compressibility at different velocities. As shown in Fig. 14, the peak value and total specific impulse of the initial impact pressure waves at Gauges 1 and 2 increase with projectile velocity. With a preset bubble, the peak pressure attenuation ratio of Gauge 1 at different velocities ranges from 21.1% to 33.9%. In comparison, the peak pressure attenuation ratio of Gauge 2 is mainly around 60%. The specific impulse attenuation ratios of the two gauges are equivalent.

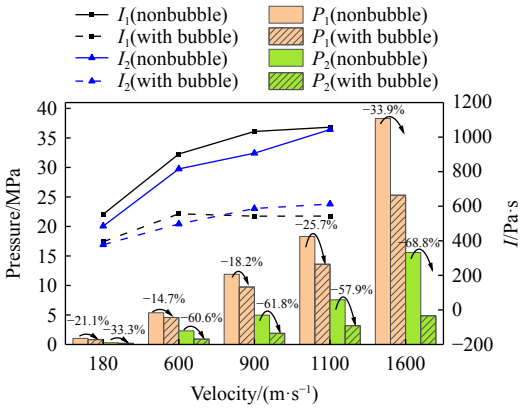

Fig.14 Peak pressure and total specific impulse of Gauges 1 and 2 at different velocities

2.2.2 Failure mode of front and rear walls

Figs. 15 and 16 depict the displacement curves of the front and rear walls at different velocities, their maximum global and local deformation, and their attenuation ratios. Tab. 2 shows the failure modes at the perforation of the rear wall at different velocities.

Since the preset bubble does not affect the stage of the projectile penetrating the front wall, the morphology of the front wall failure changes slightly and exhibits adiabatic shear failure. However, the local deformation of the front wall can be divided into two categories. For the first category, the projectile velocity is low (v = 180 m/s), the local deformation of the front wall is inward-dishing. This phenomenon is mainly caused by the low-speed impact of the projectile, which generates a small initial pressure wave peak and results in smaller reverse deformation. For the second category, the projectile velocity is high (v > 600 m/s). The dishing deformation caused by the projectile's impact gradually decreases, and the reverse deformation caused by the initial impact pressure wave increases, forming an outward reverse local deformation (Fig. 15).

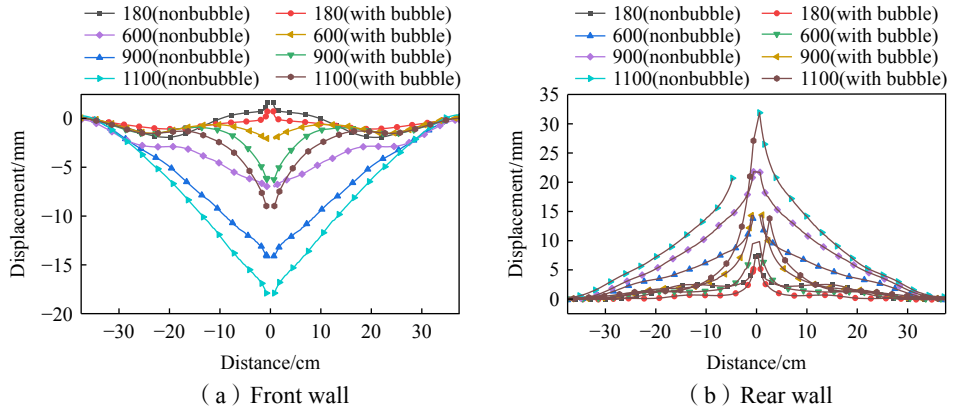

（a）Front wall （b）Rear wall

Fig.15 Centerline displacement versus distance for different velocities

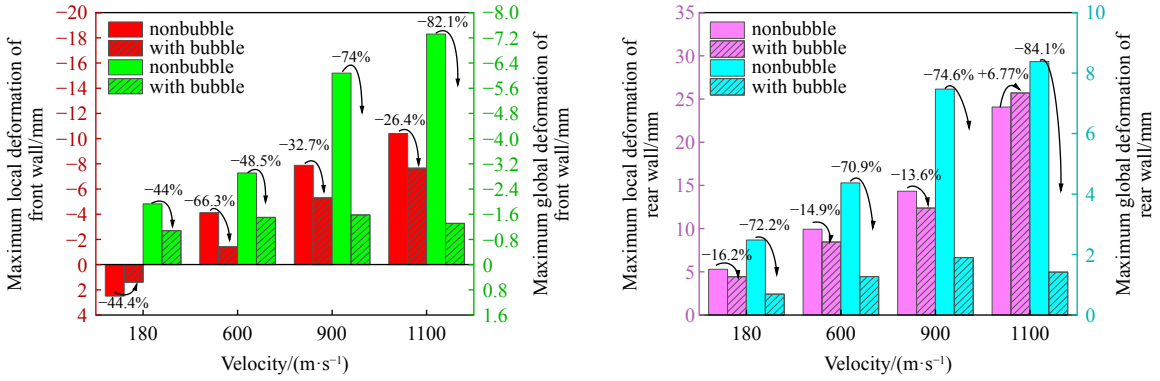

（a）Front wall （b）Rear wall

Fig.16 Effect of preset bubble on maximum deformation and attenuation ratio

Tab.2 Failure at the perforation of a rear wall under different velocities

D/mm	v/(m·s^{-1})				
	180	600	900	1100	1600
0	Bulging and tensile combined failure mode	Shearing and tensile combined failure mode	Shearing and petal cracking (4 petals) combined failure mode	Shearing and petal cracking (5 petals) combined failure mode	Petal cracking and boundary tearing combined failure mode
100	Shearing and tensile combined failure mode	Shearing and tensile combined failure mode	Shearing and petal cracking (5 petals) combined failure mode	Shearing and petal cracking (5 petals) combined failure mode	Shearing and petal cracking (6 petals) combined failure mode

As shown in Fig. 16, the preset bubble is characterized by significant attenuation on the global ddeformation of the front and rear walls. The attenuation ratio (the maximum deformation with bubble minus the maximum deformation without bubble divided by the maximum deformation without bubble) increases with velocity. On the other hand, the local deformation attenuation ratio of the front and rear walls decreases with an increase in velocity. When v = 1100 m/s, the local deformation of the rear wall relatively increases. This increase can be attributed to the projectile exiting the bubble and entering the water again, which generates a large secondary impact pressure wave and local high pressure on the rear wall. Similarly, with a preset bubble, the residual velocity of the projectile penetrating the rear wall increases, and according to the simulation results the failure at the perforation of the rear wall becomes more severe (Tab. 2). However, when v = 1600 m/s, the fluid-filled structure undergoes global tearing failure without a preset bubble. With a preset bubble, the severity of failure of the fluid-filled structure is significantly decreased, with shearing and plugging

failure of the front wall and petal failure of the rear wall. Nevertheless, the structure remained integral. In summary, a preset bubble significantly reduces the global deformation of the structure and ensures its integrity.

2.3 Influence of bubble size on attenuation characteristics

2.3.1 Analysis of pressure attenuation characteristics

Fig. 17 depicts the pressure and specific impulse time history curves of Gauges 1 and 2 under different bubble sizes. The smaller the diameter of the preset bubble, the smaller the range of influence of the rarefaction wave reflected on its surface. When its diameter is less than 50 mm and 75 mm for Gauges 1 and 2, respectively, the initial pressure wave peaks are unaffected. The smaller the diameter of the preset bubble, the larger the range of a secondary impact pressure wave. When the diameter is less than 50 mm and 25 mm for Gauges 1 and 2, respectively, they start to be significantly affected by secondary impact pressure waves. The larger the diameter of the preset bubble, the more significant the attenuation of the specific impulse.

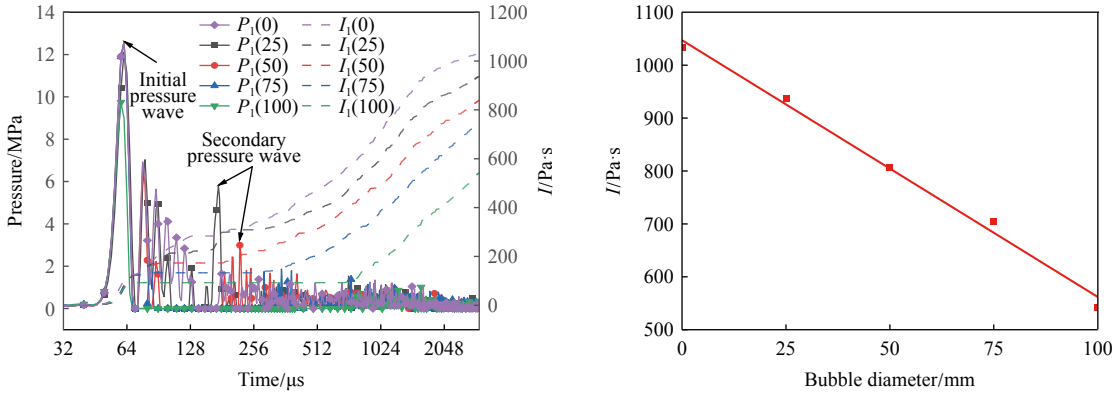

（a）Pressure Gauge 1

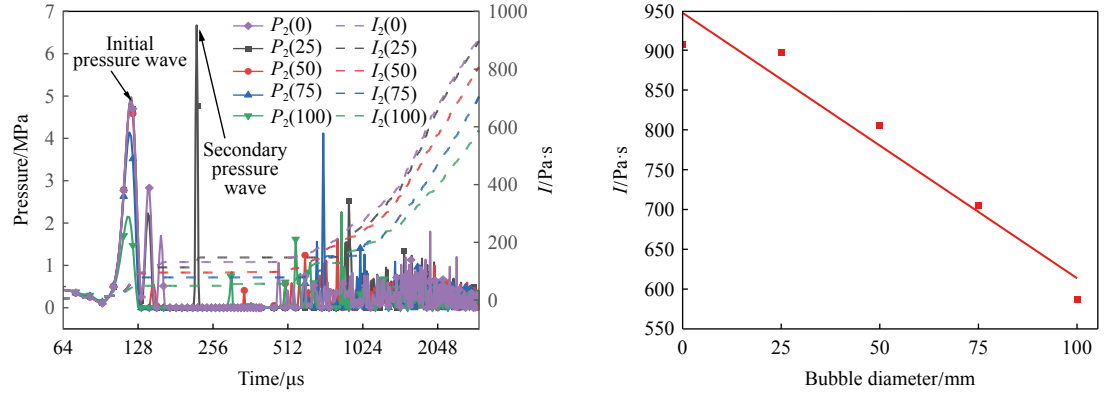

（b）Pressure Gauge 2

Fig.17 Time history of pressure and specific impulse at Gauges 1 and 2 under different bubble sizes

2.3.2 Analysis of deformation and load characteristics of front and rear walls

Fig. 18 depicts the centerline displacement curves of the front and rear walls of the fluid-filled structure under different preset bubble sizes. As shown in the figure, with an increase in bubble size, global and local deformation of the front and rear walls show a decreasing trend. Moreover, the maximum deformation of the front and rear walls decreases approximately linearly with an increase in bubble size.

Five load gauges from 9 to 13 were taken on the rear wall (Fig. 2) to analyze the influence range of preset bubble size on the initial and secondary impact pressure waves. Fig. 19 depicts the initial impact pressure wave peak value P_{f1} and the secondary impact pressure wave peak P_{f2} at Gauges 9–13 under different bubble sizes.

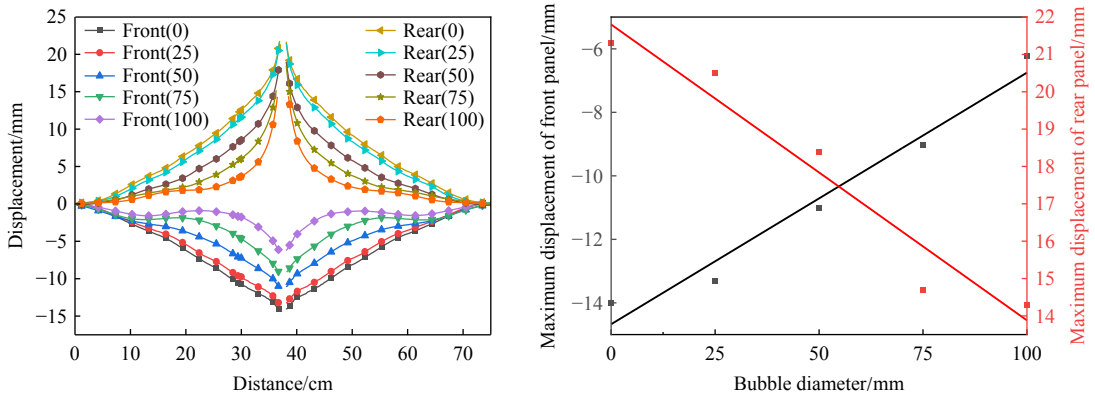

（a）Centerline displacement curves （b）Maximum values

Fig.18 Displacements of the front and rear walls for different bubble sizes

As shown in Fig. 19, the initial impact pressure wave peaks at Gauges 9–13 decrease with an increase in bubble size. The peaks of the secondary impact pressure wave at Gauges 9–10 increases with the bubble size, while it decreases at Gauges 11–13 with an increase in bubble size. Under the same bubble size, the peaks of the secondary impact pressure wave at Gauges 9–13 show a decreasing trend. At Gauges 9–12, the peaks of the secondary impact pressure wave are higher than those of the initial pressure wave; the difference between the two increases with the bubble size. At Gauge 13, the secondary impact pressure wave peaks are all smaller than those of the initial pressure wave. Moreover, the difference between the two decreases with an increase in bubble size.

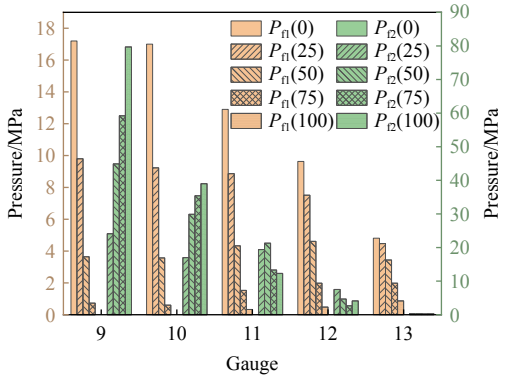

Fig.19 Peaks of initial and secondary impact pressure waves at load Gauges 9–13 under different bubble sizes

In summary, the larger the bubble, the more significant the deformation attenuation of the front and rear walls; the smaller the initial pressure wave peak value at each pressure gauge on the rear wall, the greater the influence region of the initial pressure wave acting on the rear wall, and the smaller the influence region of the secondary pressure wave. The aforementioned observations are also valid vice-versa.

3 Conclusions

The analysis presented in this paper is based on the experimental model of a spherical projectile penetrating the fluid-filled structure in Ref. [11]. The explicit dynamic analysis software LS-DYNA was adopted to conduct numerical simulation and analyze the effects of a preset bubble on the trajectory on the HRAM loads, structural deformation, and failure characteristics of the fluid-filled structure. The conclusions are as follows:

(1) With a preset bubble on the trajectory, the secondary water impact phenomenon occurs and generates the secondary impact pressure wave. Moreover, the cavity expansion process can be divided into two parts: in front of the bubble and behind the bubble. The maximum cavity size decreases, and the cavity shrinks and collapses earlier due to the compressibility of the bubble. The energy transferred from the projectile to the fluid alleviates.

(2) With a preset bubble on the trajectory, the rarefaction wave reflected on the bubble's surface can significantly attenuate the initial impact pressure wave peak value and a specific impulse in the fluid. The higher the projectile velocity and bubble size, the more obvious the attenuation effect. The peak value attenuation ratio of the initial impact pressure wave can reach 68.8%, and the total specific impulse attenuation ratio can reach 48.6%. The larger the bubble size, the greater the influence region of the initial pressure wave acting on the rear wall, and the smaller the influence region of the secondary pressure wave. The aforementioned observations are also valid vice-versa.

(3) According to the load characteristics of the front and rear walls, their deformation and failure modes can be divided into two parts: global and local. The larger the bubble, the higher the projectile velocity, and the more obvious the attenuation of global deformation and failure modes. The global deformation attenuation ratio of the front and rear walls can reach over 80%. However, the secondary projectile's impact on the water generates a significant secondary pressure wave and local high pressure on the rear wall. The larger the bubble, the faster the projectile, the smaller the local deformation and failure modes attenuation effect of the rear wall, and the more severe the failure at the perforation of the rear wall. In summary, a preset bubble significantly reduces the global deformation of the structure and ensures its integrity. However, this study does not address the function of the position and quantity of preset bubbles in attenuating HRAM loads. Therefore, further experimental and analytical investigations are necessary to provide a deep understanding of the mechanism of the preset bubbles in reducing vulnerability with respect to HRAM effects.

References

[1] Truscott T T, Techet A, Water entry of spinning spheres[J]. Journal of Fluid Mechanics, 2009, 625: 135–165.

[2] Lin J, Luo B, Xu, M, et al. Progress of aluminium projectile impacting on plate with hypervelocity[J]. Chinese Journal of High Pressure Physics, 2019, 33(3): 164–196. (in Chinese)

[3] Zou D, Hao Y, Wu H, et al. Safety assessment of large-scale all steel LNG storage tanks under wind-borne missile impact[J]. Thin-Walled Structures, 2022, 174: 109078.

[4] Disimile P J, Davis J, Toy N. Mitigation of shock waves within a liquid filled tank[J]. International Journal of Impact Engineering, 2011, 38(2/3): 61–72.

[5] Wang B, Zhang Y, Bai C, et al. Mitigating hydrodynamic ram effect by a novel perforated lattice filled tank[J]. Thin-Walled Structures, 2023, 182: 110232.

[6] Artero-Guerrero J A, Varas D, Pernas-sánchez J, et al. Experimental analysis of an attenuation method for hydrodynamic ram effects[J]. Materials & Design, 2018, 155: 451–462.

[7] Xu S, Zhang W, Cai Y, et al. Study on anti-penetration performance of Kevlar reinforced honeycomb liquid filled cabin on warship: Experimental verification and numerical analysis[J]. Ocean Engineering, 2023, 283: 114959.

[8] Gao S, Li D, Hou H, et al. Investigation on dynamic response of liquid-filled concave cell structures subject to the penetration of high-speed projectiles[J]. Thin-Walled Struct., 2020, 157: 107–119.

[9] Zhao Z, Hou H, Li D, et al, Dynamic response and protection effectiveness of fluid filled concave multicell structure under air blast[J]. Materials & Design, 2023, 229: 111876.

[10] Gao S, Zhao Z, Hou H, et al. Expansion characteristics of liquid-filled cell on hydrodynamic ram effect subject to the impact of high-speed projectile[J]. Journal of Ship Mechanics, 2023, 27(12): 1840–1855. (in Chinese)

[11] Varas D, López-Puente J, Zaera R. Experimental analysis of fluid-filled aluminium tubes subjected to high-velocity impact[J]. International Journal of Impact Engineering, 2009, 36(1): 81–91.

[12] Varas D, Zaera R, López-Puente J. Numerical modelling of the hydrodynamic ram phenomenon[J]. International Journal of Impact Engineering, 2009, 36: 363–374.

[13] Varas D, Zaera R, López-Puente J. Experimental study of CFRP fluid-filled tubes subjected to high-velocity impact[J].

Composite Structures, 2011, 93: 2598–2609.
[14] Artero-Guerrero J, Pernas-Sánchez J, López-Puente J, et al. On the influence of filling level in CFRP aircraft fuel tank subjected to high velocity impacts[J]. Composite Structures, 2014, 107: 570–577.
[15] Zhang Y, Wang B, Liu X, et al. Numerical simulation of projectile impact of liquid-filled grid structures[J]. Science Technology and Engineering, 2020, 20(19): 7689–7695. (in Chinese)
[16] Townsend D, Park N, Devall P M. Failure of fluid filled structures due to high velocity fragment impact[J]. International Journal of Impact Engineering, 2003, 29(1/2/3/4/5/6/7/8/9/10): 723–733.
[17] Li Y, Zhao P, Zhang C, et al. Influences of air-contain structure on dynamic responses of liquid-filled structures under spherical projectile penetration[J]. Journal of Vibration and Shock, 2018, 37(3): 186–194+209. (in Chinese)
[18] Jin J, Li D, Hou H, et al. Attenuation effect of a preset bubble on hydrodynamic ram induced by fragments impacting fluid-filled tank[J]. Thin-Walled Structures, 2023, 192: 111085.
[19] Li D, Zhu X, Hou H, et al. Finite element analysis of load characteristic of liquid-filled structure subjected to high velocity on long-rod projectile penetration[J]. Explosion and Shock Waves, 2016, 36(1): 1–8. (in Chinese)
[20] Xu S, Meng Z, Liu W, et al. Numerical simulation of a high-speed fragment penetrating a liquid tan[J]. Journal of Vibration and Shock, 2019, 38(6): 144–150. (in Chinese)
[21] Ji Y, Li X, Zhou L, et al. Review of study on hydrodynamic ram effect generated due to high-velocity penetrator impacting fluid-filled container[J]. Journal of Vibration and Shock, 2019, 38(19): 242–252. (in Chinese)
[22] Shen X, Zhu X, Hou H, et al. Finite element analysis of underwater high velocity fragment mushrooming and penetration properties[J]. Ship Science and Technology, 2012, 34(7): 25–29. (in Chinese)

蓄液结构内预置气泡对弹体侵彻和结构破损特性影响数值分析

吴蒙蒙[a,b], 侯海量[a], 李　典[a], 李永清[a], 夏维学[b], 杨少红[b]
（海军工程大学 a. 舰船与海洋学院; b. 基础部, 武汉 430033）

摘要: 本文探索高速弹体侵彻产生的水锤冲击载荷对蓄液结构产生的破坏以及防护技术。根据压力波在气液界面的反射、透射现象和气体的可压缩特性, 开展蓄液结构弹迹上预置气泡对弹体侵彻及结构响应特性影响的数值分析。结果表明, 当弹体轨迹上存在预设气泡时, 会发生二次入水冲击现象, 并产生二次入水冲击载荷; 在预置气泡表面反射的稀疏波使初始冲击压力峰值的衰减率达到 68.8%, 总比冲量衰减率达 48.6%; 且气泡越大, 弹体速度越高, 载荷衰减效应越明显; 由于气泡的可压缩性, 前后壁板的整体变形衰减率可达 80% 以上; 然而, 气泡尺寸越大, 弹丸速度越快, 后壁板的局部变形衰减效应越小, 后壁穿孔处的破坏越严重。

关键词: 蓄液结构; 气泡; 水锤冲击载荷; 弹体; 侵彻; 衰减
中图分类号: O342　　**文献标识码:** A
基金项目: 国家自然科学基金资助项目（52271338; 51979277; 52371342; 12102475）
作者简介: 吴蒙蒙（1991–）, 女, 博士研究生, 海军工程大学讲师;
侯海量（1977–）, 男, 博士, 海军工程大学教授。